Multi-higher-order Dirac and nodal line semimetals

Amartya Pal [1,2,*] and Arnob Kumar Ghosh [3,†]
[1]*Institute of Physics, Sachivalaya Marg, Bhubaneswar 751005, India*
[2]*Homi Bhabha National Institute, Training School Complex, Anushakti Nagar, Mumbai 400094, India*
[3]*Department of Physics and Astronomy, Uppsala University, Box 516, 75120 Uppsala, Sweden*

(Received 2 September 2024; accepted 19 May 2025; published 28 May 2025)

In recent years, there has been a surge of interest in exploring higher-order topology and their semimetallic counterparts, particularly in the context of Dirac, Weyl, and nodal line semimetals, termed higher-order Dirac semimetals (HODSM), higher-order Weyl semimetals, and higher-order nodal line semimetals (HONLSM). The HODSM phase exhibits hinge Fermi arcs (FAs) with a quantized higher-order topological invariant. Conversely, the HONLSM phase is a hybrid-order topological phase manifesting both drumhead-like surface states and hinge FAs as a signature of first- and second-order topology, and also possesses both first- and second-order topological invariants. In this work, we investigate a tight binding model for multi-HODSM (mHODSM) hosting multiple hinge FAs having a quantized quadrupolar winding number (QWN) greater than one. Furthermore, we obtain a multi-HONLSM (mHONLSM) phase from the mHODSM by applying an external magnetic field, which breaks the $\mathcal{PT}$ symmetry. The mHONLSM phase possesses both the dipolar winding number, nonvanishing only inside the nodal loops, being the representative invariant for first-order topology, and the QWN, featuring both drumhead-like surface states and multiple hinge FAs. We study the spectral properties of the mHODSM and mHONLSM in different geometries. We also investigate the hinge FA-mediated transport in HONLSM employing a two-terminal setup.

DOI: 10.1103/PhysRevB.111.195429

I. INTRODUCTION

Recent decades have witnessed profound research activities in the field of gapped and gapless topological phases of matter. Among the gapless topological phases, Dirac semimetals (DSM), Weyl semimetals (WSM) [1–17], and nodal line semimetals (NLSM) [18–27] in three spatial dimensions have been investigated extensively. At the same time, the experimental discovery of DSMs, WSMs [28–42], and NLSM [19,21,22] have prompted further interest in this area. In a DSM, the valence and conductance bands touch at isolated points in the Brillouin zone (BZ), forming Dirac nodes (DNs). Around these DNs, the energy spectrum exhibits linear dispersion in momentum hosting Dirac fermions as low-energy excitations [15]. In WSMs, the bulk is gapless at an even number of isolated points in the BZ. The topology of the WSMs is manifested at the boundary via the gapless surface states, known as Fermi arcs (FAs) [14–16]. However, in contrast to the DSM and WSM, the NLSM possesses a bulk with gapless nodal loops in the BZ. Interestingly, the nontrivial topology of NLSM results in flat drumhead-like surface states at the boundary [43,44], whereas surface states of WSMs are generally dispersive in nature. Topological protection of NLSM requires the presence of crystalline symmetries, e.g., mirror reflection, in addition to internal symmetries [18]. Nonetheless, recently a chiral symmetric NLSM phase has been proposed which does not require any crystalline symmetries except translation invariance [45,46].

Recently the discovery of higher-order topological insulators (HOTIs) has further stimulated research in topological materials [47–52]. Conventional topological insulators (TIs) in a d dimension support $(d-1)$-dimensional topologically protected boundary states [53–55]. In contrast, an nth-order HOTI in d dimensions manifests topologically protected boundary states at their $(d-n)$-dimensional boundaries [47–50]. For example, a second-order TI (SOTI) harbors zero-dimensional (0D) localized corner and one-dimensional (1D) gapless hinge states in two and three dimensions, respectively. In comparison, a third-order TI in three dimensions manifests 0D localized corner states. The notion of higher-order topology has also been transmuted into higher-order topological semimetals, namely, higher-order DSM (HODSM) [56–62], higher-order WSM (HOWSM) [63–66], and higher-order NLSM (HONLSM) [67–71]. The HODSM hosts 1D hinges states as a signature of second-order topology and is characterized by the bulk quadrupole moment [56]. On the other hand, the HOWSM embodies both first-order (conventional TIs) and second-order topological phases, manifesting a hybrid-order topology [63–66,72]. At the same time, the HONLSM exhibits bulk bands with gapless nodal loops in

*Contact author: amartya.pal@iopb.res.in
†Contact author: arnob.ghosh@physics.uu.se

the BZ, reminiscent of the bulk of NLSM [67–71]. However, in contrast to the first-order NLSM, the HONLSM hosts both the drumhead-like surface states and along with hinge FAs [67–71]. While the topological characterization of the HONLSM requires computing both the winding number or Zak phase and bulk quadrupole moment as the representative of first- and second-order topology, respectively [45,46,69–71]. The HONLSM phase has also been realized in different meta-material platforms such as acoustic setup [70] and phononic crystals [71].

Furthermore, HOTIs can also be generalized to a multi-HOTI (mHOTI) harboring multiple states per boundary [73]. The mHOTIs are protected by chiral symmetry and are topologically characterized by employing a multipole chiral winding number (MCWN) [73]. However, these mHOTIs require long-range hoppings and hence have been realized only in meta-material platforms so far [73–77]. Very recently, MCWN has been utilized to predict multi-HODSM (mHODSM) [78] where DNs are associated with MCWN and the system supports multiple FAs per hinge. However, a multi-HONLSM (mHONLSM) phase featuring MCWN and multiple hinge FAs along with drumhead surface states is yet to be reported. Moreover, having multiple hinge FAs provides us with multiple available conducting channels for FA-mediated transport [79]. Motivated by the above fact, in this work we seek the answers to the following questions: (1) Is it possible to obtain the mHONLSM phase with a higher MCWN starting from the mHODSM phase? (2) What are the signatures of mHONLSM in the band structure and at the boundary of the system? (3) Can we obtain FA-mediated enhanced conductance in a nanowire geometry consisting of mHONLSM? In this paper, we address these interesting questions.

In this work, we consider a three-dimensional (3D) tight-binding model Hamiltonian that hosts the mHODSM phase, protected by the $\mathcal{PT}$ symmetry. The Hamiltonian consists of both first- and second-nearest-neighbor hopping, while the latter is referred to as the long-range hopping throughout our paper. First, we investigate the topological phase diagram of this model employing the MCWN, in particular, the quadrupolar winding number (QWN) $\mathcal{N}_{xy}$. We analyze the bulk Fermi surface featuring the DNs of the bulk Hamiltonian and also for a system with semi-infinite geometries. Next, we break the $\mathcal{PT}$ symmetry by applying an external magnetic field to the mHODSM, which in turn transmutes the system to the mHONLSM. We observe that the nodal points of the mHODSM phase get inflated into nodal loops resembling the nature of NLSM. Interestingly, the system also posses chiral symmetry, and we compute the dipolar winding number (DWN) $\mathcal{W}$ to characterize the first-order topology and the QWN $\mathcal{N}_{xy}$ to characterize the second-order topology of the mHONLSM phase. We obtain two kinds of mHONLSM phases with (1) $\mathcal{N}_{xy} = 1, 4$ and $\mathcal{W} = -1$ and (2) $\mathcal{N}_{xy} = 4$ and $\mathcal{W} = -1$. We analyze the band structure of these two kinds of mHONLSM phases in different geometries. We also explore the FA-mediated transport properties of mHONLSM by employing a two-terminal setup.

The remainder of the paper is organized as follows. In Sec. II we introduce the tight-binding model for the mHODSM phase and study the corresponding phase diagram and band structures. Section III is devoted to the main results of this paper, where we discuss the mHONLSM phase and characterize it by computing $\mathcal{W}$ and $\mathcal{N}_{xy}$. We study the band structure of the mHONLSM and also investigate the FA-mediated conductance signature employing a two-terminal setup. Finally, we summarize our article and provide a brief outlook in Sec. IV.

II. mHODSM

In this section we introduce the model Hamiltonian exhibiting the mHODSM phase. We topologically characterize the phase using QWN and obtain the phase diagram. Afterward, we analyze the band structure of the system in different geometries.

A. Model Hamiltonian

We consider a model for the 3D mHODSM, which consists of stacking of 2D SOTI layers along the z direction [50,78,80]. The system can be described by the following tight binding Hamiltonian on a cubic lattice as

$$\begin{aligned}\mathcal{H}(\mathbf{k}) &= \lambda_1(\sin k_x\Gamma_1 + \sin k_y\Gamma_2) + (m - t_x\cos k_x - t_y\cos k_y)\Gamma_3 + \Delta(\cos k_x - \cos k_y)\Gamma_4 \\ &+ (\lambda_2 + t_z\cos k_z)[\sin 2k_x\Gamma_1 + \sin 2k_y\Gamma_2 - (\cos 2k_x + \cos 2k_y)\Gamma_3 + (\cos 2k_x - \cos 2k_y)\Gamma_4], \end{aligned} \tag{1}$$

where, t_x, t_y, and t_z represent the nearest-neighbor hopping amplitudes along the x, y, and z directions, respectively. The on-site crystal field splitting, spin-orbit coupling, and Wilson-Dirac (WD) mass term are denoted by m, λ_1, and Δ, respectively [50,80]. The terms associated with λ_2 generate the long-range hopping along the x and y directions. The 4×4 $\mathbf{\Gamma}$ matrices are chosen as $\Gamma_1 = \sigma_1 s_3$, $\Gamma_2 = \sigma_2 s_0$, $\Gamma_3 = \sigma_3 s_0$, and $\Gamma_4 = \sigma_1 s_1$, where the Pauli matrices $\boldsymbol{\sigma}$ and $\mathbf{s}$ act on the orbital and spin subspace, respectively. The WD mass term is important to obtain higher-order topology in the system. For $\lambda_2, t_z = 0$, the Hamiltonian represents 2D SOTI hosting 0D corner modes for $m < |t_x + t_y|$. On the other hand, $\lambda_2 \neq 0$ and $t_z = 0$ also represent a 2D SOTI, but with next-nearest-neighbor hopping [81]. In this case the SOTI model also represents a multi-SOTI that supports multiple modes per corner [81]. At the same time, a nonzero t_z allows coupling between two stacked SOTI layers. When $\Delta \neq 0$, the Hamiltonian $\mathcal{H}(\mathbf{k})$ breaks TRS $\mathcal{T} = i\sigma_0 s_2 \mathcal{K}$: $\mathcal{T}\mathcal{H}(\mathbf{k})\mathcal{T}^{-1} \neq \mathcal{H}(-\mathbf{k})$, inversion symmetry $\mathcal{P} = \sigma_3 s_0$: $\mathcal{P}\mathcal{H}(\mathbf{k})\mathcal{P}^{-1} \neq \mathcal{H}(-\mathbf{k})$, and the fourfold rotational symmetry around the z axis $C_4 = e^{-\frac{i\pi}{4}\sigma_3 s_3}$: $C_4\mathcal{H}(\mathbf{k})C_4^{-1} \neq \mathcal{H}(-k_y, k_x, k_z)$, with $\mathcal{K}$ being the complex conjugation

operator. However, $\mathcal{H}(\mathbf{k})$ preserves the combined $\mathcal{PT}$ symmetry $PT = \mathcal{PT} = i\sigma_3 s_2 \mathcal{K}$: $(PT)\mathcal{H}(\mathbf{k})(PT)^{-1} = \mathcal{H}(\mathbf{k})$. Thus, the system supports fourfold degenerate $\mathcal{PT}$-symmetric DNs [72]. Additionally, $\mathcal{H}(\mathbf{k})$ preserves the combined $C_4\mathcal{T}$ symmetry: $(C_4\mathcal{T})\mathcal{H}(\mathbf{k})(C_4\mathcal{T})^{-1} = \mathcal{H}(k_y, -k_x, -k_z)$. Importantly, $\mathcal{H}(\mathbf{k})$ also respects chiral symmetry $\mathcal{S} = \sigma_1 s_2$: $\mathcal{S}\mathcal{H}(\mathbf{k})\mathcal{S}^{-1} = -\mathcal{H}(\mathbf{k})$. Here chiral symmetry plays a crucial role in defining the QWN, which we employ to topologically characterize the phase. Without loss of generality, we consider $\lambda_1 = t_x = t_y = \Delta = \lambda_2 = 1$ and $t_z = 2$ for the rest of the paper. Nevertheless, our analysis is not affected by this specific choice of parameters.

B. Topological invariant and phase diagram

Having introduced the model Hamiltonian, we now study the topological phase diagram of the mHODSM. The HODSM phase embodies the signature of second-order topology as it constitutes the stacking of 2D SOTI layers, possessing nontrivial quadrupole moment [72]. However, for a mHODSM, the quadrupole moment vanishes due to the presence of multiple hinge states [73]. Nevertheless, the Hamiltonian $\mathcal{H}(\mathbf{k})$ [Eq. (1)] preserves chiral symmetry, and we utilize the chiral symmetry-based QWN to topologically characterize the mHODSM [73]. Here we briefly provide an outline of how to compute the QWN.

In this work, we consider stacking of 2D SOTI layers in the z direction [see Eq. (1)]. To compute the QWN, we consider a 3D system that is finite but obeys periodic boundary conditions (PBC) in the x and y directions but infinite in the z direction. We represent the Hamiltonian in the semi-infinite geometry by the symbol $\mathcal{H}(k_z)$. The Hamiltonian $\mathcal{H}(k_z)$ respects the chiral symmetry generated by S. Here S represents the chiral symmetry operator in the semi-infinite geometry and is constructed from $\mathcal{S}$ employing the same basis for $\mathcal{H}(k_z)$. We can represent $\mathcal{H}(k_z)$ in an antidiagonal form by considering the basis U_S, that diagonalizes the operator S as $U_S S U_S^\dagger = \mathrm{diag}(1, 1, \ldots, 1, -1, -1, \ldots, -1)$. In this basis $\mathcal{H}$ reads

$$\tilde{\mathcal{H}}(k_z) = U_S \mathcal{H}(k_z) U_S^\dagger = \begin{pmatrix} 0 & h(k_z) \\ h^\dagger(k_z) & 0 \end{pmatrix}. \tag{2}$$

The chiral symmetry divides the system into two sublattice degrees of freedom A and B corresponding to $+1$ and -1 eigenvalues of S, respectively. Here $S = U_A^S - U_B^S$; with $U_A^S = \sum |A\rangle \langle A|$ and $U_B^S = \sum |B\rangle \langle B|$. Now we perform a singular value decomposition of $h(k_z)$ such that $h(k_z) = U_A \Sigma U_B^\dagger$, where the matrix Σ contains the singular values and $U_{A,B}$ represent a matrix containing singular vectors. We utilize $U_{A,B}$ and $U_{A,B}^S$ to define the QWN as [73]

$$\mathcal{N}_{xy} = \frac{1}{2\pi i} \mathrm{Tr} \ln(\bar{Q}_A \bar{Q}_B^\dagger), \tag{3}$$

where $\bar{Q}_{A,B}$ are sublattice quadrupole operator, defined as $\bar{Q}_{A,B} = U_{A,B}^\dagger U_{A,B}^S Q U_{A,B}^S U_{A,B}^\dagger$ with the quadrupole operator reads as $Q = \exp(-2\pi i xy/L_x L_y)$. Here $L_x(L_y)$ represent system's dimension in the $x(y)$ direction. We employ $\mathcal{N}_{xy}$ in Eq. (3) to topologically characterize the mHODSM phase and later the mHONLSM phase as well.

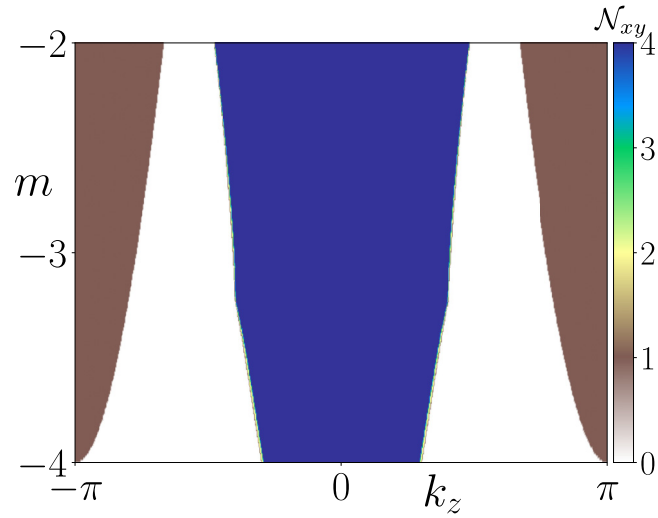

FIG. 1. Phase diagram of mHODSM in terms of the QWN $\mathcal{N}_{xy}$, is depicted in the m-k_z plane. The colorbar represents the value of $\mathcal{N}_{xy}$. We consider $L_x = L_y = 30$.

Upon introducing $\mathcal{N}_{xy}$, we now focus on the phase diagram of mHODSM. In particular, we compute $\mathcal{N}_{xy}$ in the k_z-m plane and show the same in Fig. 1. We observe that $\mathcal{N}_{xy}$ take values 1 and 4. Here $\mathcal{N}_{xy} = 4$ indicates the mHODSM with multiple hinge FAs [78]. Upon investigating the phase diagram Fig. 1, we identify two types of mHODSM phases: at $m = -4$, we observe a phase with only $\mathcal{N}_{xy} = 4$. At the same time, for any other values of m, $\mathcal{N}_{xy}$ takes values 1 and 4, which vary as a function of k_z. Nevertheless, to gain more insights into the different mHODSM phases, we focus on two different values of m: $m = -2$ and -4, and study the band structure and the features of the mHODSM in different geometries. We emphasize that the presence of chiral symmetry is necessary to characterize the topological phase with $\mathcal{N}_{xy}$ greater than one [73].

C. Band structures and signature of mHODSM

Case I, $m = -2$: Here, we concentrate on a single line at $m = -2$ in the phase diagram Fig. 1 and demonstrate the results in Fig. 2. In particular, in Fig. 2(a) we illustrate the bulk Fermi surface, i.e., the zero-energy excitations of the Hamiltonian, $\mathcal{H}(\mathbf{k})$, in Eq. (1). We observe that the valence and the conduction bands touch each other at ten isolated DNs in the BZ with the location of DNs being $(k_x, k_y, k_z) = (\pi \pm \frac{\pi}{3}, \pi \pm \frac{\pi}{3}, \pm\frac{\pi}{2})$, $(\pi, \pi, \pm\frac{2\pi}{3})$. We also explicitly show the linear dispersion of the bulk around one of the DNs at $(\pi, \pi, \frac{2\pi}{3})$ in the inset of Fig. 2(a) resembling the feature of Dirac cones. Next, we compute the band structure of the system in slab geometry, i.e., we consider an open boundary condition (OBC) along the x direction and PBC along the y and z directions to understand the surface states. Fixing $k_y = \pi$, we show the band structure in slab geometry in Fig. 2(b). We see the existence of surface states connecting the DNs. We can see such surface states in a first-order DSM also [12]. At the same time, a 3D HODSM possesses the features of SOTI. To probe the same, we consider rod geometry such that the system obeys OBC along the

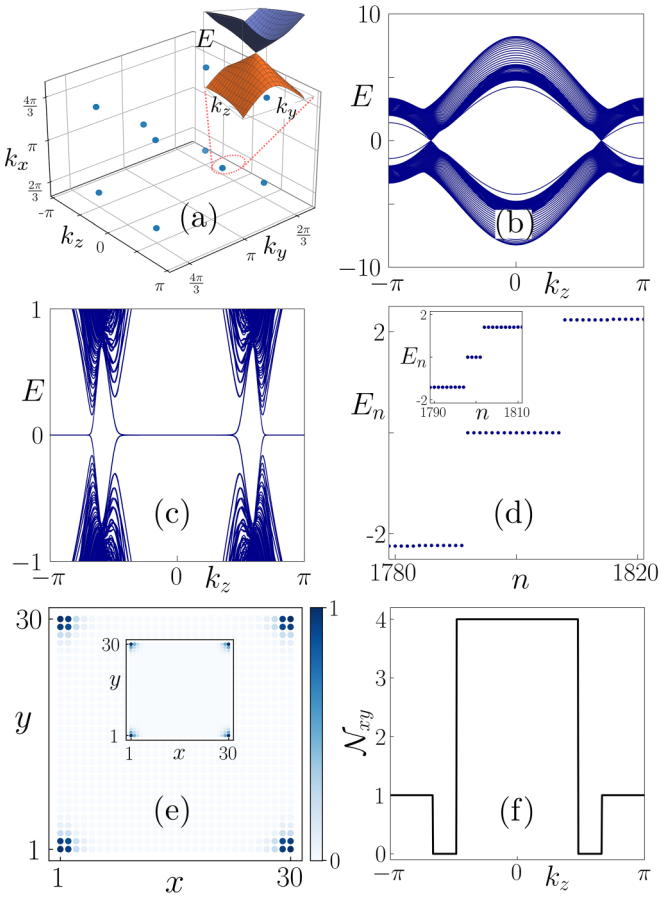

FIG. 2. (a) Bulk Fermi surface of HODSM consisting of ten DNs at $(k_x, k_y, k_z) = (\pi \pm \frac{\pi}{3}, \pi \pm \frac{\pi}{3}, \pm\frac{\pi}{2})$, $(\pi, \pi, \pm\frac{2\pi}{3})$ is shown in the (k_x-k_y-k_z) space. In the inset, we illustrate the linear band dispersion in the k_y-k_z plane around the DN located at $(\pi, \pi, \frac{2\pi}{3})$. (b) Band structure of the system in slab geometry as a function of k_z with OBC along the x direction ($L_x = 60$) and fixing $k_y = \pi$. (c) Band structure in rod geometry as a function of k_z with OBCs along the x and y direction. (d) Eigenvalue spectrum, E_n, is shown as a function of state index, n, corresponding to $k_z = 0$ in (c). Inset represents E_n vs n for $k_z = \pi$ in (c). (e) LDOS for the zero-energy states in (d). (f) $\mathcal{N}_{xy}$ is plotted as a function of k_z. For (c)–(f) we choose $L_x = L_y = 30$ and $m = -2$ for all the panels.

x and y directions and PBC along the z direction such that the system is infinite in the stacking direction. We demonstrate the band structure as a function of k_z employing rod geometry in Fig. 2(c). From Fig. 2(c) we see the existence of hinge FAs. However, we observe hinge FAs that are divided into two segments and separated by gaps. To understand the number of states in these two segments, we choose a slice from Fig. 2(c) fixing $k_z = 0$ and plot the eigenvalue spectrum E_n as a function of the eigenvalue index m in Fig. 2(d). We observe 16 states close to zero energy, implying four FAs per hinge. In the inset of Fig. 2(d), we show the eigenvalue E_n vs n for $k_z = \pi$, and we notice four states at zero energy corresponding to a single FA per hinge. Afterward, we investigate the normalized local density of states (LDOS) of these hinge FA eigenvalues at zero energy. On this account, we show the LDOS of the zero-energy states as a function of the system's dimension in the x and y directions, for $k_z = 0$ in Fig. 2(e). We can identify that the FAs are localized at the corner of the 2D cross section plane perpendicular to the stacking direction (z direction) of the system, implying the FAs are the hinge states. In the inset of Fig. 2(e), we show the LDOS of the hinge FAs at $k_z = \pi$, which again suggests localization of the FAs at the hinges of the system. Having discussed the band structure of the mHODSM and boundary signatures of the FAs, we associate a topological invariant with them. In particular, we compute QWN $\mathcal{N}_{xy}$ defined in Eq. (3) as a function of k_z and depict the same in Fig. 2(f). The QWN $\mathcal{N}_{xy}$ take the values 0, 1, and 4 as a function of k_z, which apparently matches with the flat FAs that appear at zero energy in Fig. 2(c). Here a nonzero $\mathcal{N}_{xy}$ signifies the existence of hinge FAs, with $\mathcal{N}_{xy} = 1$ signifies one FA per hinge and $\mathcal{N}_{xy} = 4$ implies the presence of four FAs per hinge. The existence of more than one FAs per hinge with $\mathcal{N}_{xy} \geqslant 1$ is a signature of the mHODSM [78].

Case II, $m = -4$: Here we discuss another mHODSM phase that is accessible from the phase diagram Fig. 1. We show the bulk Fermi surface consisting of nine DNs as shown in Fig. 3(a). Location of the DNs are $(k_x, k_y, k_z) = (\pi, \pi, \pi)$, $(\pi \pm k_{x0}, \pi \pm k_{y0}, \pm k_{z0})$ with $k_{x0} = k_{y0} \simeq 1.318$, $k_{z0} \simeq 1.047$. [The DNs located at (π, π, π) and $(\pi, \pi, -\pi)$ are equivalent.] We depict the linearly dispersing Dirac cone around the DN (π, π, π) in the inset of Fig. 3(a). The surface states are shown in Fig. 3(b) as a function of k_z with $k_y = \pi$. Moreover, we plot the rod geometry band structure in Fig. 3(c) as a function of k_z for a system obeying OBCs along the x and y directions. In contrast to the previous case, we observe only a single set of degenerate hinge FAs here. To know the degeneracy of the FAs, we also plot the eigenvalue spectrum at $k_z = 0$ in Fig. 3(d). We notice 16 modes at zero energy, signifying four FAs per hinge. To verify the hinge localization of the FAs, we show the LDOS associated with the zero-energy states in Fig. 3(e). We see that the FAs are localized at the hinges of the system. Moreover, we compute the $\mathcal{N}_{xy}$ as a function of k_z in Fig. 3(f). Here $\mathcal{N}_{xy}$ takes a value of 4 for the k_z points, which supports the hinge FAs and thereby corroborates the second-order topological nature of the system.

In summary, in this section we establish, by considering a stacking of SOTI Hamiltonians with long-range hopping in the z direction that the system supports a mHODSM with multiple hinge FAs. We show two kinds of mHODSM in Figs. 2 (one and four hinge FAs) and 3 (only four hinge FAs), with the multiple hinge FAs being topologically characterized employing the QWN.

III. mHONLSM

This section is devoted to the main results of this work. Here we discuss the mHONLSM with multiple hinge FAs along with drumhead-like surface states. To this end we first introduce the Hamiltonian that embodies the mHONLSM. The mHONLSM phase being a hybrid-order topological phase, we topologically characterize the phase employing both the DWN and the QWN. Next, we discuss the band structure in bulk, slab, and rod geometry. We also study the transport properties of the hinge FAs of the system using two-terminal conductance.

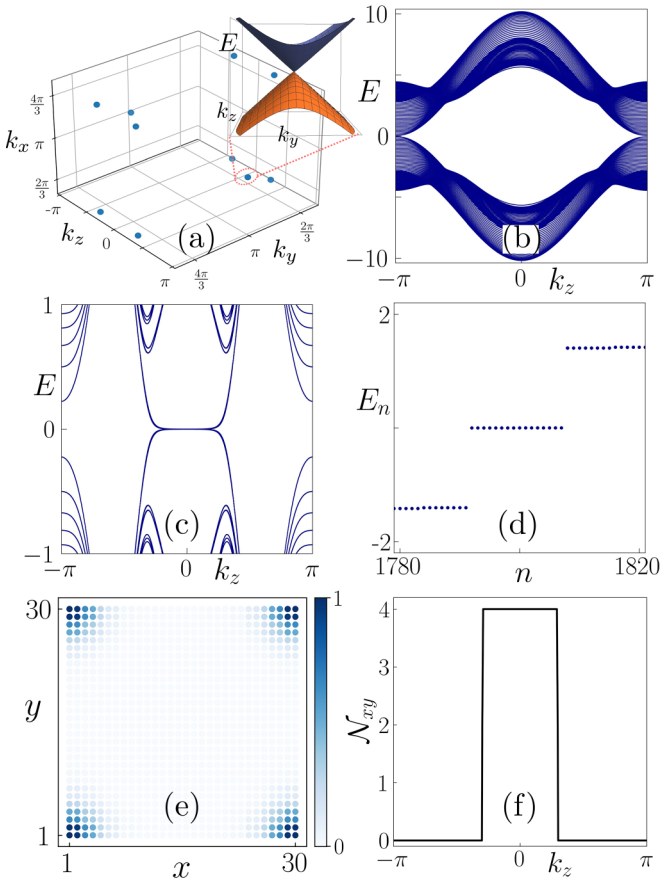

FIG. 3. (a) Bulk Fermi surface of HODSM consisting of nine DNs at $(k_x, k_y, k_z) = (\pi, \pi, \pm\pi)$, $(\pi \pm k_{x0}, \pi \pm k_{y0}, \pm k_{z0})$ is shown in the $(k_x$-k_y-$k_z)$ space with $k_{x0} = k_{y0} \simeq 1.318$, $k_{z0} \simeq 1.047$ [the DNs located at (π, π, π) and $(\pi, \pi, -\pi)$ are equivalent]. In the inset, we show the Dirac cone around the DN (π, π, π) in the k_y-k_z plane. (b) Band structure of the system in slab geometry as a function of k_z with OBC along the x direction ($L_x = 60$) and at $k_y = \pi$. (c) Band structure in rod geometry as a function of k_z with OBC along the x and y direction. (d) Eigenvalue spectrum, E_n as a function of state index n for $k_z = 0$ in (c). (e) LDOS for the zero-energy states in (d). (f) $\mathcal{N}_{xy}$ is plotted as a function of k_z. For (c)–(f), we choose $L_x = L_y = 30$ and $m = -4$ for all the panels.

A. Model Hamiltonian

In the literature, there exist various proposals for the realization of the first-order NLSMs. Conventionally, the NLSMs are protected by some crystalline symmetries [18], internal symmetries [26,27], or even only chiral symmetry [45,46]. In our case the model Hamiltonian that we employ in Eq. (1) breaks the explicit TRS but rather respects the $\mathcal{PT}$ symmetry and chiral symmetry. We obtain the mHONLSM phase by breaking the $\mathcal{PT}$ symmetry explicitly while preserving the chiral symmetry. To break the $\mathcal{PT}$ symmetry, we apply an external magnetic field along the negative x direction, such that the total Hamiltonian reads

$$\mathcal{H}'(\mathbf{k}) = \mathcal{H}(\mathbf{k}) - B_x \Lambda, \tag{4}$$

where $\Lambda = \sigma_0 s_1$. Here the Hamiltonian $\mathcal{H}'(\mathbf{k})$ breaks the $\mathcal{PT}$ symmetry such that $(PT)\mathcal{H}'(\mathbf{k})(PT)^{-1} \neq \mathcal{H}'(\mathbf{k})$. Due to the broken $\mathcal{PT}$ symmetry, the DNs of HODSM inflates into nodal loops in mHONLSM. Note that we consider only the coupling of the external magnetic field with spin degrees of freedom of the electrons [9,14,16]. Furthermore, the external magnetic field also breaks the combined $C_4\mathcal{T}$ symmetry. However, the Hamiltonian $\mathcal{H}'(\mathbf{k})$ continues to satisfy the chiral symmetry S, which allows us to topologically characterize the system based on chiral symmetry. We consider the Hamiltonian $\mathcal{H}'(\mathbf{k})$ for the topological characterization and also to obtain the signature of the mHONLSM in different geometries.

B. Topological invariant and phase diagram

Conventionally, topological protection of first-order NLSMs is demonstrated by associating a winding number [45,46] with each of the nodal loops. To point out the first-order topological nature of our system, we indulge in characterizing the phase using the DWN $\mathcal{W}$, which is used to characterize the chiral symmetric first-order topological phase [82,83], which we outline below. Note that the DWN is utilized to characterize the first-order topology in a 1D system. In our case we obtain an effective 1D system along the x direction while treating values of k_y and k_z as the parameters. This allows us to compute the DWN as a function of k_y, k_z and other parameters of the model Hamiltonian. We compute the DWN using the similar prescription mentioned for QWN (see Sec. II B) [82]. To this end, we consider the system to be finite in the x direction but obeys PBC. Now, employing the basis in which the chiral symmetry operator is diagonal, we can recast $\mathcal{H}'(k_y, k_z)$ as

$$\tilde{\mathcal{H}}'(k_y, k_z) = \begin{pmatrix} 0 & h'(k_y, k_z) \\ h'^{\dagger}(k_y, k_z) & 0 \end{pmatrix}. \tag{5}$$

As discussed in the previous section, we perform a singular value decomposition of $h'(k_y, k_z)$: $h'(k_y, k_z) = U'_A \Sigma' U'^{\dagger}_B$ with Σ' containing the singular values and $U'_{A,B}$ being the singular vectors. Now we can define the DWN as [82]

$$\mathcal{W} = \frac{1}{2\pi i} \mathrm{Tr} \ln(\bar{P}_A \bar{P}_B^{\dagger}), \tag{6}$$

where $\bar{P}_A$ and $\bar{P}_B$ are the sublattice dipole moment operator restricted to the sublattice A and B, respectively, and defined as $\bar{P}_{A,B} = U'^{\dagger}_{A,B} U'^{S\dagger}_{A,B} P U'^{S}_{A,B} U'_{A,B}$ with the dipole moment operator $P = \exp(-2\pi i x/L_x)$. Here L_x represents the system size along the x direction. The matrices $U'^{S}_{A,B}$ are defined in the same way as done in Sec. II B. However, the dimensions of these matrices are now different (less) compared to the previous case (Sec. II B) as we consider an effective 1D system. In addition to the first-order topology, the mHONLSM also exhibits the second-order topology [72]. Thus, to fully characterize the mHONLSM, we need to compute both the $\mathcal{W}$ and $\mathcal{N}_{xy}$.

We compute $\mathcal{W}$ and $\mathcal{N}_{xy}$ and illustrate them in the m-k_z plane in Figs. 4(a) and 4(b), respectively. In Fig. 4(a) we notice the appearance of a regime with $\mathcal{W} = -1$, which suggests the existence of first-order topology. Note that in Fig. 4(a) we fix $k_y = \pi$, to show the behavior of $\mathcal{W}$ in the m-k_z plane. In the next subsection, choosing particular strengths of m, we fully explore the first-order topology of mHONLSM in the k_y-k_z plane. In addition to $\mathcal{W}$, N_{xy} also acquires nonzero values of 1 and 4, as shown in Fig. 4(b).

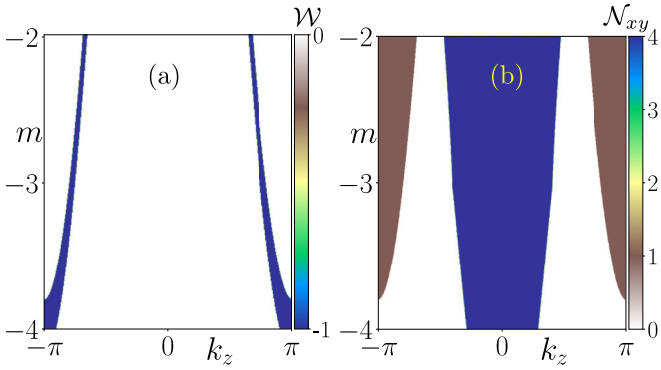

FIG. 4. (a) The DWN $\mathcal{W}$ is shown in the m-k_z plane. We fix $k_y = \pi$ and consider $L_x = 60$. (b) The QWN $\mathcal{N}_{xy}$ is depicted in the m-k_z plane. We consider $L_x = L_y = 30$. Here $B_x = 0.2$ in both the panels.

Interestingly, for each value of m, the nonzero values of $\mathcal{W}$ and N_{xy} are separated in k_z. At this point, we also mention that if we apply the external magnetic field in the positive x direction, we observe overlapping regions of $\mathcal{W}$ and N_{xy} in the m-k_z plane. Nonetheless, the coexistence of $\mathcal{W}$ and N_{xy} suggest a mHONLSM phase with a hybrid-order topology. Furthermore, in Fig. 4(b) the N_{xy} also takes values which is greater than one, implying a mHONLSM phase. Similar to the mHODSM, the mHONLSM phase is also divided into two parts: mHONLSM with $N_{xy} = 1, 4$ and $N_{xy} = 4$ only. To shine further light on these two different kinds of mHONLSM, we choose two values of $m = -2$ and -4, and we discuss the band structures in different geometries in the next subsection.

C. Band structures and signature of mHONLSM

Case I, $m = -2$: Considering a fixed value of $m = -2$ from the phase diagram Fig. 4, we first investigate the bulk band structure of mHONLSM in Fig. 5(a). We observe each of the DNs in Fig. 2(a) gets inflated into nodal loops totaling ten nodal loops in Fig. 5(a). Concentrating on the nodal loop centered around $(\pi, \pi, \frac{2\pi}{3})$, we explicitly illustrate the nature of bulk bands in the k_y-k_z plane fixing $k_x = \pi$ in the inset of Fig. 5(a). This affirms that the bulk of the Hamiltonian [Eq. (4)] indeed represent the signature of NLSM. Now, to see the boundary manifestation of the mHONLSM, we first investigate the drumhead-like surface states being the signature of NLSMs. On this account, we consider slab geometry by employing PBC along the y and z directions and OBC along the x direction (with system size $L_x = 60$). In Fig. 5(b) we plot surface states at the zero energy in the k_y-k_z plane associated with the highlighted nodal loop in Fig. 5(a) exhibiting a "Fermi drumhead." Thus, from Fig. 5(b), we can infer that the mHONLSM phase manifests drumhead-like surface states. Furthermore, we focus on a particular value of $k_y = \pi$ [shown by a dashed line in Fig. 5(b)] and show the band structure of the system in slab geometry in Fig. 5(c) and observe the flat dispersionless surface states at zero energy. Moreover,

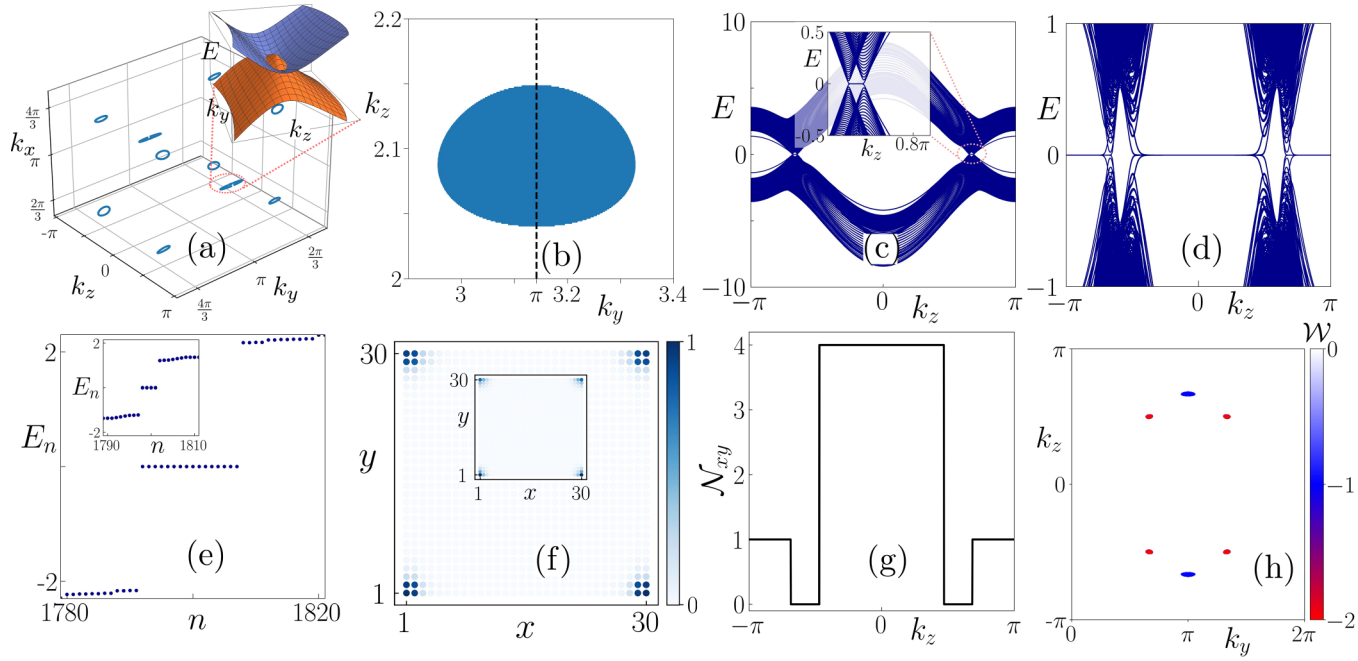

FIG. 5. (a) Bulk Fermi surface of mHONLSM comprised of ten nodal loops is shown in the (k_x-k_y-k_z) space. In the inset, we show the band structure for the nodal loop centered at $(\pi, \pi, 2\pi/3)$ in the k_y-k_z plane fixing $k_x = \pi$. (b) We illustrate the drumhead-like surface states, i.e., the zero-energy states corresponding to the nodal loop highlighted in (a) in the k_y-k_z plane employing slab geometry with finite system size along the x direction taking $L_x = 60$. (c) Band structure in the slab geometry as a function of k_z with OBC along the x direction ($L_x = 60$) and fixing $k_y = \pi$, corresponding to the black dashed line in (b). (d) Band structure in the rod geometry as a function of k_z with OBC along the x and y direction. (e) Eigenvalue spectrum E_n as a function of state index n for $k_z = 0$ in (d), while the inset corresponds to $k_z = \pi$. (f) The LDOS associated with the zero-energy states in (e) is shown as a function of the system's dimension. (g) The QWN $\mathcal{N}_{xy}$ is plotted as a function of k_z. (h) DWN $\mathcal{W}$, is shown in the (k_y-k_z) plane assuming the x direction to be finite with $L_x = 60$. For (d)–(g) we choose $L_x = L_y = 30$. We fix $m = -2$ and $B_x = 0.2$ for all the panels.

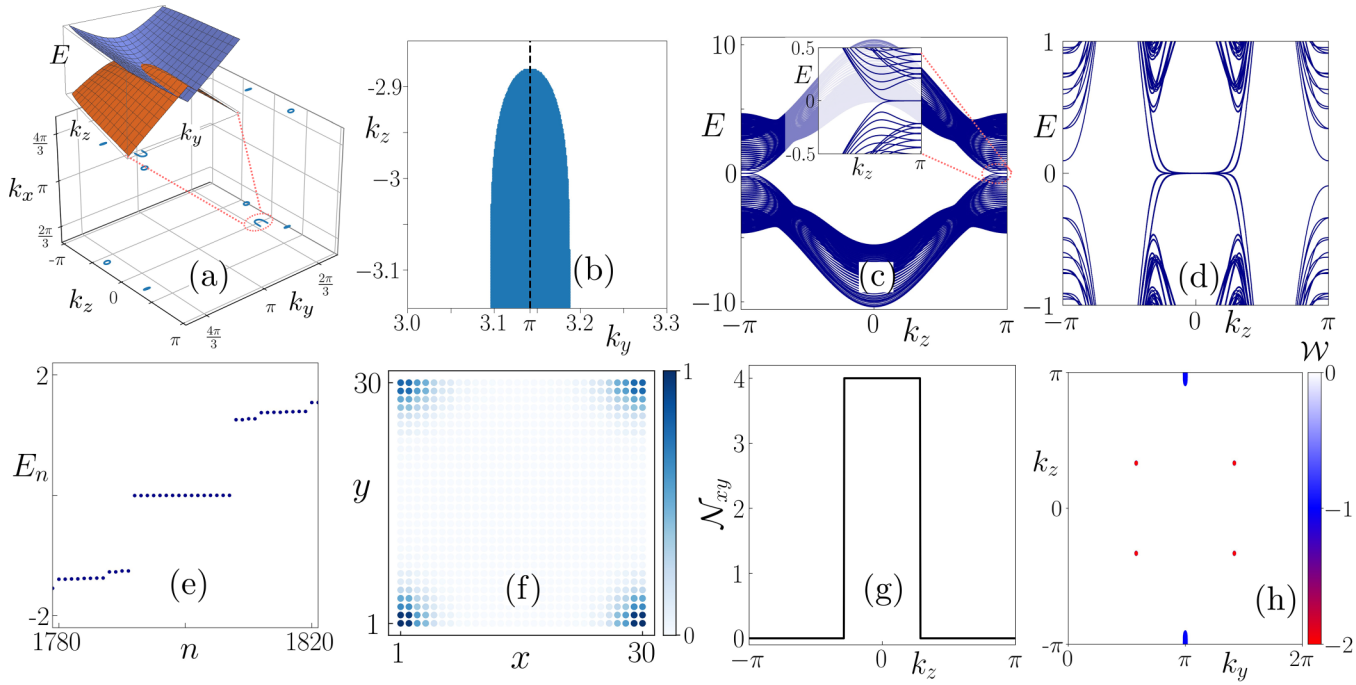

FIG. 6. (a) Bulk Fermi surface of the mHONLSM comprising of nine nodal loops is shown in the (k_x-k_y-k_z) space. In the inset, we demonstrate the band structure for nodal loops centered at (π, π, π) in the k_y-k_z plane fixing $k_x = \pi$. (b) Illustration of drumhead-like surface states in the k_y-k_z plane with finite system size along the x direction ($L_x = 60$), corresponding to the nodal loop highlighted in (a). (c) Band structure in the slab geometry as a function of k_z with OBC along x direction ($L_x = 60$) and fixing $k_y = \pi$, corresponding to the black dashed line in (b). (d) Band structure in the rod geometry as a function of k_z with OBC along the x and y direction. (e) Eigenvalue spectrum, E_n, is shown as a function of state index n, corresponding to $k_z = 0$ in (d), while the inset corresponds to $k_z = \pi$. (f) The LDOS associated with the zero-energy states in (e) is shown as a function of the system's dimension. (g) The QWN $\mathcal{N}_{xy}$ is plotted as a function of k_z. (h) DWN $\mathcal{W}$, is shown in the k_y-k_z plane assuming the x direction to be finite with $L_x = 60$. For (d)–(g), we choose $L_x = L_y = 30$. We fix $m = -4$ and $B_x = 0.2$ for all the panels.

the mHONLSM phase also possesses the characteristics of second-order topology, manifesting hinge FAs. To resolve this, we consider rod geometry by employing OBC along the x and y directions (with system size $L_x = L_y = 30$) and PBC along the z direction. We demonstrate the band structure in rod geometry in Fig. 5(d). We observe the hinge FAs as the states at $E = 0$, and the FAs are divided into two segments. We note that the surface FAs are gapped out in rod geometry due to finite size effect as already established in literature [79,84–87]. Nevertheless, to understand the number of hinge FAs in each segment, we show the eigenvalue spectrum E_n as a function of the eigenvalue index n in rod geometry for fixed values of $k_z = 0$ in Fig. 5(e) and $k_z = \pi$ in the inset. We notice 16 eigenvalues at $E_n = 0$ i.e., four FAs per hinge and four eigenvalues at $E_n = 0$ i.e., one FA per hinge in Fig. 5(e) and its inset, respectively. To further corroborate the location of the FAs, we also compute the LDOS associated with these FAs appearing at zero energy and show them in Fig. 5(f). From Fig. 5(f) and its inset, we can identify that the FAs are localized at the hinges of the system. Having investigated the emergence of the mHONLSM phase from the spectral analysis, we now study the corresponding topological invariants as discussed before. In particular, we show the $\mathcal{N}_{xy}$ as a function of k_z in Fig. 5(g). Here $\mathcal{N}_{xy}$ shows a jump between 0, 1, and 4 and follows a similar structure as the hinge FAs shown in Fig. 5(d). Nevertheless, the $\mathcal{N}_{xy}$ values greater than one signify a mHONLSM phase. Furthermore, to fully explore the first-order topology of mHONLSM, we also plot the DWN $\mathcal{W}$ in the k_y-k_z plane in Fig. 5(h). We observe the DWN $\mathcal{W}$ takes values -1 and -2. Interestingly, the regions with nonzero values of $\mathcal{W}$ indicate the presence of topological nodal loops, and $\mathcal{W}$ is nonzero only inside the nodal loops. Here $\mathcal{W} = -1$ and $\mathcal{W} = -2$ signify the presence of single and double nodal loops, respectively, when projected onto the k_y-k_z plane.

Case II, $m = -4$: Similar to the previous case, we show another mHONLSM phase by fixing another value of $m = -4$. We illustrate the bulk Fermi surface structure in Fig. 6(a) featuring nine nodal loops at zero located at zero energy. We also plot the bulk band structure corresponding to the nodal loop centered at (π, π, π). The drum head surface states at $E = 0$ is shown in Fig. 6(b) in the k_y-k_z plane employing the slab geometry. In Fig. 6(c), we illustrate the surface states as a function of k_z fixing $k_y = \pi$ [corresponding to the dashed black line in Fig. 6(b)]. In Fig. 6(d) we demonstrate the rod geometry band structure featuring the hinge FAs. Here we observe only one type of hinge FAs in contrast to the previous case [see Fig. 5(d)]. For a fixed value of $k_z = 0$, we show the eigenvalue spectrum E_n as a function of the state index n in Fig. 6(e). We see 16 zero-energy modes corresponding to four states per hinge. The LDOS associated with the zero-energy states are shown in Fig. 6(f), corroborating the hinge localization of the zero-energy states. In Fig. 6(g) we exhibit the QWN $\mathcal{N}_{xy}$ as a function of k_z where $\mathcal{N}_{xy}$ takes

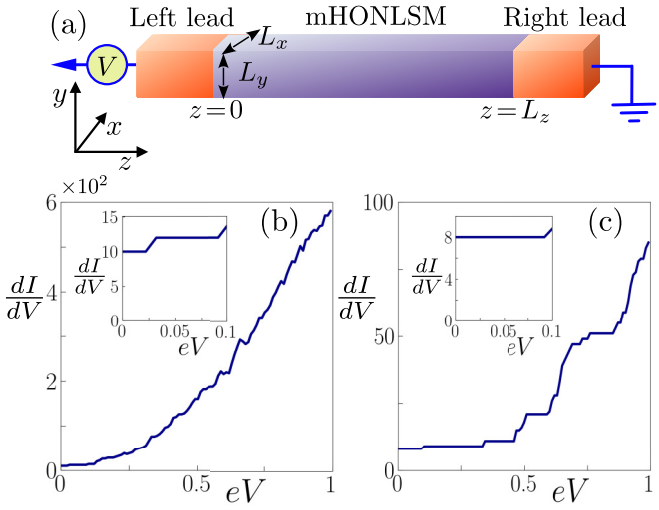

FIG. 7. (a) The two terminal transport setup consisting of the mHONLSM as the device (middle blue region) and two mHONLSM leads. (b), (c) Differential conductance $\frac{dI}{dV}$ (in units of e^2/h) as a function of the bias voltage eV for $m=-2$ (corresponding to Fig. 5) and $m=-4$ (corresponding to Fig. 6), respectively. The device region has the dimensions $L_x=L_y=30$, and $L_z=80$. The inset shows $\frac{dI}{dV}$ close to $eV=0$. The rest of the parameters take the same value as Fig. 5.

the values 0 and 4. The higher values of $\mathcal{N}_{xy}(\geqslant 1)$ signifies a mHONLSM phase. In Fig. 6(h) $\mathcal{W}$ is shown in the k_y-k_z plane. Similar to the $m=-2$ case, here $\mathcal{W}$ takes two nonzero values i.e., -1 and -2, signifying the presence of single and double nodal loops, respectively, projected onto the k_y-k_z plane. The nonzero DWN $\mathcal{W}$ is the manifestation of first-order topology in the system.

Note that, in the rod geometry band structure [Figs. 5(d) and 6(d)], the first-order surface FA states are gapped out due to the quantum confinement effect, whereas the second-order hinge localized states are gapless and present at the zero energy states. Therefore, utilizing the band structure in slab and rod geometry, we can distinguish between the first- and second-order FAs. On the other hand, the hinge FAs that we obtain are dispersionless i.e., flat in nature, and thus do not carry any chirality [63].

D. Two-terminal transport

The significance of mHONLSM over NLSM and WSM becomes most evident when studying the transport properties in a nanowire (NW) geometry. The FA surface states of a NLSM and WSM are gapped out in an NW due to the quantum confinement in a finite system [79,84–89]. As a result, no states are available to conduct current if Fermi energy lies in the middle of the band. In contrast, in a mHONLSM, the existence of gapless hinge modes in the NW geometry leads to a nonzero density of states at Fermi energy, thereby contributing to the transport signature. The differential conductance near the Fermi energy is solely given by the number of hinge states that are present in the system. To this end, we consider a two-terminal transport setup as shown in Fig. 7(a), comprising the mHONLSM as the device (blue; from $z=0$ to $z=L_z$) and two leads (orange), which are also considered to be mHONLSM, so that there is no mismatch of bands of the leads and device. We employ the Landauer formalism to compute the differential conductance $\frac{dI}{dV}$ as [90]

$$\frac{dI}{dV}=\frac{e^2}{h}\mathcal{T}_{\mathrm{LR}}(V_{\mathrm{L}}-V_{\mathrm{R}}), \tag{7}$$

where $\frac{e^2}{h}$ defines the unit of quantum conductance and $\mathcal{T}_{\mathrm{LR}}(V_{\mathrm{L}}-V_{\mathrm{R}})$ represents the transmission probability from left to the right lead at a voltage bias $(V_{\mathrm{L}}-V_{\mathrm{R}})$. The right lead in our setup is grounded $(V_{\mathrm{R}}=0)$, and we apply a voltage bias in the left lead $(V_{\mathrm{L}}=V)$. We compute the differential conductance as a function of the voltage difference between the left and the right lead $eV=(V_{\mathrm{L}}-V_{\mathrm{R}})$. We employ the python package KWANT to calculate the transmission probability $\mathcal{T}_{\mathrm{LR}}$ [91].

We show the differential conductance $\frac{dI}{dV}$ (in units of e^2/h) as a function of the bias voltage difference eV for the two kinds of mHONLSM shown in Figs. 5 and 6 and in Figs. 7(b) and 7(c), respectively. In particular, we first focus on Fig. 7(b) (corresponding to Fig. 5). In the inset, we show the $\frac{dI}{dV}$ close to Fermi energy. At zero bias $eV=0$, we observe that the differential conductance takes a quantized value of 10. To understand this, we investigate Figs. 5(d) and 5(e), which exhibits two kinds of hinge states: four and one states per hinge, totaling 20 conducting channels available from all the hinges. However, in Fig. 7(b) we show only the conductance for bias voltage $eV\geqslant 0$. Thus, we only obtain the contribution from half of the number of available channels, which justifies the quantized differential conductance at $eV=0$ to be 10. Moreover, in Fig. 7(c) we study the transport properties of the hinge FAs of the mHONLSM phase shown in Fig. 6. From the inset, we observe a quantized differential conductance of 8 at zero bias $(eV=0)$, which corresponds to a total of 16 hinge FA channels available in this phase [see Figs. 6(d) and 6(e)]. Nevertheless, from Figs. 7(b) and 7(c), we establish that, in the NW geometry, we obtain the contribution from the hinge FAs to the zero bias differential conductance. Moreover, the differential conductance of the mHODSM in the NW geometry will behave similarly to the mHONLSM phase as both phases host an equal number of hinge localized modes. Since the first-order Fermi surfaces are gapped out, they will not contribute to the zero-bias conductance in the transport measurement.

In summary, in this section, we show the emergence of the mHONLSM phase by breaking the $\mathcal{PT}$ symmetry in mHODSM. We show two kinds of mHONLSM phase in Fig. 5 (one and four FAs per hinge) and Fig. 6 (only four FAs per hinge). We compute the QWN to characterize the multiple hinge FAs and the DWN to characterize the drumhead-like Fermi surface. By computing the two terminal conductance, we also show the hinge FAs mediated differential conductance. On the other hand, the presence of multiple hinge FAs is beneficial for obtaining a high value of conductance at Fermi energy.

IV. SUMMARY AND OUTLOOK

To summarize, in this work we consider a tight binding model as the stacking of 2D SOTIs with long-range hopping

to obtain an mHODSM phase, which exhibits multiple FAs per hinge. We employ the QWN $\mathcal{N}_{xy}$ to obtain the phase diagram. Furthermore, we focus on two specific parameters exhibiting two different kinds of mHODSM and plot the DNs in the k_x-k_y-k_z space and also illustrate corresponding band structures in different geometries. Afterward, we break the $\mathcal{PT}$ symmetry by applying a magnetic field to obtain the mHONLSM. To probe the hybrid order topology in the mHONLSM phase, we compute both the QWN $\mathcal{N}_{xy}$ and the DWN $\mathcal{W}$ and draw the phase diagram. Akin to the mHODSM phase, we also find two kinds of mHONLSM phase: one with $\mathcal{N}_{xy} = 1, 4$ and the other with $\mathcal{N}_{xy} = 4$ only. We show the nodal loops in the k_x-k_y-k_z space and study drumhead-like surface states and hinge FAs employing slab and rod geometry, respectively. We also demonstrate that the DWN is finite inside the nodal loops and zero otherwise. We further employ a two-terminal transport setup to obtain the hinge FA-mediated signature as a quantized conductance at Fermi energy.

In this work, long-range hopping plays a crucial role in obtaining the mHODSM and mHONLSM phases. Thus, we can also ask if we can obtain the mHODSM and mHONLSM phases without needing long-range hopping. Driven systems can be a suitable platform to engineer this. Since we can generate long-range hopping in a driven system [92], it creates a possibility to obtain the mHODSM and mHONLSM phases in a driven system without starting with a system with long-range hopping. Moreover, in a driven system, we can also have the possibility to break the $\mathcal{PT}$ symmetry without needing the magnetic field [72].

ACKNOWLEDGMENTS

We are grateful for the fruitful discussions with Arijit Saha and Tanay Nag. A.P. also acknowledges Faruk Abdullah, Krishanu Roychowdhury, and Soujanya Dutta for useful discussions. A.P. acknowledges SAMKHYA: High-Performance Computing facility provided by the Institute of Physics, Bhubaneswar, for numerical computations.

DATA AVAILABILITY

The data that support the findings of this article are openly available [93].

[1] X. Wan, A. M. Turner, A. Vishwanath, and S. Y. Savrasov, Topological semimetal and Fermi-arc surface states in the electronic structure of pyrochlore iridates, Phys. Rev. B **83**, 205101 (2011).

[2] A. A. Burkov and L. Balents, Weyl semimetal in a topological insulator multilayer, Phys. Rev. Lett. **107**, 127205 (2011).

[3] A. A. Burkov, M. D. Hook, and L. Balents, Topological nodal semimetals, Phys. Rev. B **84**, 235126 (2011).

[4] S. M. Young, S. Zaheer, J. C. Y. Teo, C. L. Kane, E. J. Mele, and A. M. Rappe, Dirac semimetal in three dimensions, Phys. Rev. Lett. **108**, 140405 (2012).

[5] A. A. Zyuzin, S. Wu, and A. A. Burkov, Weyl semimetal with broken time reversal and inversion symmetries, Phys. Rev. B **85**, 165110 (2012).

[6] A. A. Zyuzin and A. A. Burkov, Topological response in Weyl semimetals and the chiral anomaly, Phys. Rev. B **86**, 115133 (2012).

[7] G. B. Halász and L. Balents, Time-reversal invariant realization of the Weyl semimetal phase, Phys. Rev. B **85**, 035103 (2012).

[8] C.-X. Liu, P. Ye, and X.-L. Qi, Chiral gauge field and axial anomaly in a Weyl semimetal, Phys. Rev. B **87**, 235306 (2013).

[9] M. M. Vazifeh and M. Franz, Electromagnetic response of Weyl semimetals, Phys. Rev. Lett. **111**, 027201 (2013).

[10] T. Bzdušek, A. Rüegg, and M. Sigrist, Weyl semimetal from spontaneous inversion symmetry breaking in pyrochlore oxides, Phys. Rev. B **91**, 165105 (2015).

[11] S. Rao, Weyl semi-metals: A short review, J. Indian Inst. Sci. **96**, 145 (2016).

[12] M. Kargarian, M. Randeria, and Y.-M. Lu, Are the surface Fermi arcs in Dirac semimetals topologically protected? Proc. Natl. Acad. Sci. USA **113**, 8648 (2016).

[13] B. Yan and C. Felser, Topological materials: Weyl semimetals, Annu. Rev. Condens. Matter Phys. **8**, 337 (2017).

[14] T. M. McCormick, I. Kimchi, and N. Trivedi, Minimal models for topological Weyl semimetals, Phys. Rev. B **95**, 075133 (2017).

[15] N. P. Armitage, E. J. Mele, and A. Vishwanath, Weyl and Dirac semimetals in three-dimensional solids, Rev. Mod. Phys. **90**, 015001 (2018).

[16] U. Khanna, A. Kundu, S. Pradhan, and S. Rao, Proximity-induced superconductivity in Weyl semimetals, Phys. Rev. B **90**, 195430 (2014).

[17] A. Burkov, Weyl metals, Annu. Rev. Condens. Matter Phys. **9**, 359 (2018).

[18] C.-K. Chiu and A. P. Schnyder, Classification of reflection-symmetry-protected topological semimetals and nodal superconductors, Phys. Rev. B **90**, 205136 (2014).

[19] G. Bian, T.-R. Chang, R. Sankar, S.-Y. Xu, H. Zheng, T. Neupert, C.-K. Chiu, S.-M. Huang, G. Chang, I. Belopolski *et al.*, Topological nodal-line fermions in spin-orbit metal $PbTaSe_2$, Nat. Commun. **7**, 10556 (2016).

[20] A. Yamakage, Y. Yamakawa, Y. Tanaka, and Y. Okamoto, Line-node Dirac semimetal and topological insulating phase in noncentrosymmetric pnictides CaAgX (X = P, As), J. Phys. Soc. Jpn. **85**, 013708 (2016).

[21] Y.-H. Chan, C.-K. Chiu, M. Y. Chou, and A. P. Schnyder, Ca_3P_2 and other topological semimetals with line nodes and drumhead surface states, Phys. Rev. B **93**, 205132 (2016).

[22] S. Nie, H. Weng, and F. B. Prinz, Topological nodal-line semimetals in ferromagnetic rare-earth-metal monohalides, Phys. Rev. B **99**, 035125 (2019).

[23] S.-Y. Yang, H. Yang, E. Derunova, S. S. P. Parkin, B. Yan, and M. N. Ali, Symmetry demanded topological nodal-line materials, Adv. Phys.: X **3**, 1414631 (2018).

[24] F. Parhizgar and A. M. Black-Schaffer, Large Josephson current in Weyl nodal loop semimetals due to odd-frequency superconductivity, npj Quantum Mater. **5**, 42 (2020).

[25] J. Zhan, J. Li, W. Shi, X.-Q. Chen, and Y. Sun, Coexistence of Weyl semimetal and Weyl nodal loop semimetal phases in a collinear antiferromagnet, Phys. Rev. B **107**, 224402 (2023).

[26] S. Matsuura, P.-Y. Chang, A. P. Schnyder, and S. Ryu, Protected boundary states in gapless topological phases, New J. Phys. **15**, 065001 (2013).

[27] Y. X. Zhao and Z. D. Wang, Topological classification and stability of Fermi surfaces, Phys. Rev. Lett. **110**, 240404 (2013).

[28] G. Xu, H. Weng, Z. Wang, X. Dai, and Z. Fang, Chern semimetal and the quantized anomalous Hall effect in $HgCr_2Se_4$, Phys. Rev. Lett. **107**, 186806 (2011).

[29] A. C. Potter, I. Kimchi, and A. Vishwanath, Quantum oscillations from surface Fermi arcs in Weyl and Dirac semimetals, Nat. Commun. **5**, 5161 (2014).

[30] B. Q. Lv, N. Xu, H. M. Weng, J. Z. Ma, P. Richard, X. C. Huang, L. X. Zhao, G. F. Chen, C. E. Matt, F. Bisti *et al.*, Observation of Weyl nodes in TaAs, Nat. Phys. **11**, 724 (2015).

[31] B. Q. Lv, H. M. Weng, B. B. Fu, X. P. Wang, H. Miao, J. Ma, P. Richard, X. C. Huang, L. X. Zhao, G. F. Chen *et al.*, Experimental discovery of Weyl semimetal TaAs, Phys. Rev. X **5**, 031013 (2015).

[32] B. Q. Lv, S. Muff, T. Qian, Z. D. Song, S. M. Nie, N. Xu, P. Richard, C. E. Matt, N. C. Plumb, L. X. Zhao *et al.*, Observation of Fermi-arc spin texture in TaAs, Phys. Rev. Lett. **115**, 217601 (2015).

[33] S.-Y. Xu, I. Belopolski, D. S. Sanchez, C. Zhang, G. Chang, C. Guo, G. Bian, Z. Yuan, H. Lu, T.-R. Chang *et al.*, Experimental discovery of a topological Weyl semimetal state in TaP, Sci. Adv. **1**, e1501092 (2015).

[34] S.-Y. Xu, N. Alidoust, I. Belopolski, Z. Yuan, G. Bian, T.-R. Chang, H. Zheng, V. N. Strocov, D. S. Sanchez, G. Chang *et al.*, Discovery of a Weyl fermion state with Fermi arcs in niobium arsenide, Nat. Phys. **11**, 748 (2015).

[35] S.-Y. Xu, I. Belopolski, N. Alidoust, M. Neupane, G. Bian, C. Zhang, R. Sankar, G. Chang, Z. Yuan, C.-C. Lee *et al.*, Discovery of a Weyl fermion semimetal and topological Fermi arcs, Science **349**, 613 (2015).

[36] L. Lu, Z. Wang, D. Ye, L. Ran, L. Fu, J. D. Joannopoulos, and M. Soljačić, Experimental observation of Weyl points, Science **349**, 622 (2015).

[37] Y. Sun, S.-C. Wu, and B. Yan, Topological surface states and Fermi arcs of the noncentrosymmetric Weyl semimetals TaAs, TaP, NbAs, and NbP, Phys. Rev. B **92**, 115428 (2015).

[38] A. A. Soluyanov, D. Gresch, Z. Wang, Q. Wu, M. Troyer, X. Dai, and B. A. Bernevig, Type-II Weyl semimetals, Nature (London) **527**, 495 (2015).

[39] Z. Wang, D. Gresch, A. A. Soluyanov, W. Xie, S. Kushwaha, X. Dai, M. Troyer, R. J. Cava, and B. A. Bernevig, $MoTe_2$: A type-II Weyl, Phys. Rev. Lett. **117**, 056805 (2016).

[40] L.-X. Wang, C.-Z. Li, D.-P. Yu, and Z.-M. Liao, Aharonov–Bohm oscillations in Dirac semimetal Cd_3As_2 nanowires, Nat. Commun. **7**, 10769 (2016).

[41] P. J. W. Moll, N. L. Nair, T. Helm, A. C. Potter, I. Kimchi, A. Vishwanath, and J. G. Analytis, Transport evidence for Fermi-arc-mediated chirality transfer in the Dirac semimetal Cd_3As_2, Nature (London) **535**, 266 (2016).

[42] S.-Y. Xu, I. Belopolski, D. S. Sanchez, M. Neupane, G. Chang, K. Yaji, Z. Yuan, C. Zhang, K. Kuroda, G. Bian *et al.*, Spin polarization and texture of the Fermi arcs in the Weyl fermion semimetal TaAs, Phys. Rev. Lett. **116**, 096801 (2016).

[43] G. Bian, T.-R. Chang, H. Zheng, S. Velury, S.-Y. Xu, T. Neupert, C.-K. Chiu, S.-M. Huang, D. S. Sanchez, I. Belopolski *et al.*, Drumhead surface states and topological nodal-line fermions in $TlTaSe_2$, Phys. Rev. B **93**, 121113 (2016).

[44] H. Weng, Y. Liang, Q. Xu, R. Yu, Z. Fang, X. Dai, and Y. Kawazoe, Topological node-line semimetal in three-dimensional graphene networks, Phys. Rev. B **92**, 045108 (2015).

[45] F. Abdulla, G. Murthy, and A. Das, Topological nodal line semimetals with chiral symmetry, arXiv:2311.18667.

[46] F. Abdulla, G. Murthy, and A. Das, Stable nodal line semimetals in the chiral classes in three dimensions, arXiv:2401.02966.

[47] W. A. Benalcazar, B. A. Bernevig, and T. L. Hughes, Quantized electric multipole insulators, Science **357**, 61 (2017).

[48] W. A. Benalcazar, B. A. Bernevig, and T. L. Hughes, Electric multipole moments, topological multipole moment pumping, and chiral hinge states in crystalline insulators, Phys. Rev. B **96**, 245115 (2017).

[49] Z. Song, Z. Fang, and C. Fang, $(d-2)$-dimensional edge states of rotation symmetry protected topological states, Phys. Rev. Lett. **119**, 246402 (2017).

[50] F. Schindler, A. M. Cook, M. G. Vergniory, Z. Wang, S. S. Parkin, B. A. Bernevig, and T. Neupert, Higher-order topological insulators, Sci. Adv. **4**, eaat0346 (2018).

[51] S. Manna, S. Nandy, and B. Roy, Higher-order topological phases on fractal lattices, Phys. Rev. B **105**, L201301 (2022).

[52] A. K. Ghosh, T. Nag, and A. Saha, Generation of higher-order topological insulators using periodic driving, J. Phys.: Condens. Matter **36**, 093001 (2024).

[53] C. L. Kane and E. J. Mele, Quantum spin Hall effect in graphene, Phys. Rev. Lett. **95**, 226801 (2005).

[54] B. A. Bernevig and S.-C. Zhang, Quantum spin Hall effect, Phys. Rev. Lett. **96**, 106802 (2006).

[55] B. A. Bernevig, T. L. Hughes, and S.-C. Zhang, Quantum spin Hall effect and topological phase transition in HgTe quantum wells, Science **314**, 1757 (2006).

[56] M. Lin and T. L. Hughes, Topological quadrupolar semimetals, Phys. Rev. B **98**, 241103 (2018).

[57] B. J. Wieder, Z. Wang, J. Cano, X. Dai, L. M. Schoop, B. Bradlyn, and B. A. Bernevig, Strong and fragile topological Dirac semimetals with higher-order Fermi arcs, Nat. Commun. **11**, 627 (2020).

[58] W. Wu, Z.-M. Yu, X. Zhou, Y. X. Zhao, and S. A. Yang, Higher-order Dirac fermions in three dimensions, Phys. Rev. B **101**, 205134 (2020).

[59] H. Qiu, M. Xiao, F. Zhang, and C. Qiu, Higher-order Dirac sonic crystals, Phys. Rev. Lett. **127**, 146601 (2021).

[60] Z. Wang, D. Liu, H. T. Teo, Q. Wang, H. Xue, and B. Zhang, Higher-order Dirac semimetal in a photonic crystal, Phys. Rev. B **105**, L060101 (2022).

[61] R. Chen, B. Zhou, and D.-H. Xu, Quasicrystalline second-order topological semimetals, Phys. Rev. B **108**, 195306 (2023).

[62] S. M. Rafi-Ul-Islam, Z. B. Siu, H. Sahin, and M. B. A. Jalil, Chiral surface and hinge states in higher-order Weyl semimetallic circuits, Phys. Rev. B **109**, 085430 (2024).

[63] S. A. A. Ghorashi, T. Li, and T. L. Hughes, Higher-order Weyl semimetals, Phys. Rev. Lett. **125**, 266804 (2020).

[64] H.-X. Wang, Z.-K. Lin, B. Jiang, G.-Y. Guo, and J.-H. Jiang, Higher-order Weyl semimetals, Phys. Rev. Lett. **125**, 146401 (2020).

[65] W. B. Rui, Z. Zheng, M. M. Hirschmann, S.-B. Zhang, C. Wang, and Z. D. Wang, Intertwined Weyl phases emergent from higher-order topology and unconventional Weyl fermions via crystalline symmetry, npj Quantum Mater. **7**, 15 (2022).

[66] Y. Tanaka, R. Takahashi, R. Okugawa, and S. Murakami, Rotoinversion-symmetric bulk-hinge correspondence and its applications to higher-order Weyl semimetals, Phys. Rev. B **105**, 115119 (2022).

[67] Z. Wang, B. J. Wieder, J. Li, B. Yan, and B. A. Bernevig, Higher-order topology, monopole nodal lines, and the origin of large Fermi arcs in transition metal dichalcogenides $X\mathrm{Te}_2$ (X = Mo, W), Phys. Rev. Lett. **123**, 186401 (2019).

[68] K. Wang, J.-X. Dai, L. B. Shao, S. A. Yang, and Y. X. Zhao, Boundary criticality of $\mathcal{PT}$-invariant topology and second-order nodal-line semimetals, Phys. Rev. Lett. **125**, 126403 (2020).

[69] C. Chen, X.-T. Zeng, Z. Chen, Y. X. Zhao, X.-L. Sheng, and S. A. Yang, Second-order real nodal-line semimetal in three-dimensional graphdiyne, Phys. Rev. Lett. **128**, 026405 (2022).

[70] H. Qiu, Y. Li, Q. Zhang, and C. Qiu, Discovery of higher-order nodal surface semimetals, Phys. Rev. Lett. **132**, 186601 (2024).

[71] Q. Ma, Z. Pu, L. Ye, J. Lu, X. Huang, M. Ke, H. He, W. Deng, and Z. Liu, Observation of higher-order nodal-line semimetal in phononic crystals, Phys. Rev. Lett. **132**, 066601 (2024).

[72] Z.-M. Wang, R. Wang, J.-H. Sun, T.-Y. Chen, and D.-H. Xu, Floquet Weyl semimetal phases in light-irradiated higher-order topological Dirac semimetals, Phys. Rev. B **107**, L121407 (2023).

[73] W. A. Benalcazar and A. Cerjan, Chiral-symmetric higher-order topological phases of matter, Phys. Rev. Lett. **128**, 127601 (2022).

[74] D. Wang, Y. Deng, J. Ji, M. Oudich, W. A. Benalcazar, G. Ma, and Y. Jing, Realization of a $\mathbb{Z}$-classified chiral-symmetric higher-order topological insulator in a coupling-inverted acoustic crystal, Phys. Rev. Lett. **131**, 157201 (2023).

[75] H. Liu, X. Huang, M. Yan, J. Lu, W. Deng, and Z. Liu, Acoustic topological metamaterials of large winding number, Phys. Rev. Appl. **19**, 054028 (2023).

[76] Y. Li, J.-H. Zhang, F. Mei, B. Xie, M.-H. Lu, J. Ma, L. Xiao, and S. Jia, Large-chiral-number corner modes in $\mathbb{Z}$-class higher-order topolectrical circuits, Phys. Rev. Appl. **20**, 064042 (2023).

[77] Y. Li, H. Qiu, Q. Zhang, and C. Qiu, Acoustic higher-order topological insulators protected by multipole chiral numbers, Phys. Rev. B **108**, 205135 (2023).

[78] Y. Qi, Z. He, K. Deng, J. Li, and Y. Wang, Multipole higher-order topological semimetals, Phys. Rev. B **109**, L060101 (2024).

[79] A. Pal, P. Dutta, and A. Saha, Fermi arc mediated transport in an inversion symmetry broken Weyl semimetal nanowire and its hybrid junctions, Phys. Rev. B **109**, 235419 (2024).

[80] D. Călugăru, V. Juričić, and B. Roy, Higher-order topological phases: A general principle of construction, Phys. Rev. B **99**, 041301 (2019).

[81] A. K. Ghosh, A. Saha, and T. Nag, Corner modes in non-Hermitian next-nearest-neighbor hopping model, Phys. Rev. B **110**, 115403 (2024).

[82] L. Lin, Y. Ke, and C. Lee, Real-space representation of the winding number for a one-dimensional chiral-symmetric topological insulator, Phys. Rev. B **103**, 224208 (2021).

[83] D. Mondal, A. K. Ghosh, T. Nag, and A. Saha, Topological characterization and stability of Floquet Majorana modes in Rashba nanowires, Phys. Rev. B **107**, 035427 (2023).

[84] V. Kaladzhyan and J. H. Bardarson, Quantized Fermi arc mediated transport in Weyl semimetal nanowires, Phys. Rev. B **100**, 085424 (2019).

[85] A. Igarashi and M. Koshino, Magnetotransport in Weyl semimetal nanowires, Phys. Rev. B **95**, 195306 (2017).

[86] B.-C. Lin, S. Wang, L.-X. Wang, C.-Z. Li, J.-G. Li, D. Yu, and Z.-M. Liao, Gate-tuned Aharonov-Bohm interference of surface states in a quasiballistic Dirac semimetal nanowire, Phys. Rev. B **95**, 235436 (2017).

[87] S. Wang, B.-C. Lin, W.-Z. Zheng, D. Yu, and Z.-M. Liao, Fano interference between bulk and surface states of a Dirac semimetal Cd_3As_2 nanowire, Phys. Rev. Lett. **120**, 257701 (2018).

[88] E. V. Gorbar, V. A. Miransky, I. A. Shovkovy, and P. O. Sukhachov, Origin of dissipative Fermi arc transport in Weyl semimetals, Phys. Rev. B **93**, 235127 (2016).

[89] G. Chen, W. Chen, and O. Zilberberg, Field-effect transistor based on surface negative refraction in Weyl nanowire, APL Mater. **8**, 011102 (2020).

[90] S. Datta, *Electronic Transport in Mesoscopic Systems* (Cambridge University Press, Cambridge, 1997).

[91] C. W. Groth, M. Wimmer, A. R. Akhmerov, and X. Waintal, Kwant: A software package for quantum transport, New J. Phys. **16**, 063065 (2014).

[92] T. Mikami, S. Kitamura, K. Yasuda, N. Tsuji, T. Oka, and H. Aoki, Brillouin-Wigner theory for high-frequency expansion in periodically driven systems: Application to Floquet topological insulators, Phys. Rev. B **93**, 144307 (2016).

[93] A. Pal and A. K. Ghosh, Data for "Multi-higher-order Dirac and nodal line semimetals," (Version v3) [Data set], Zenodo (2025), https://doi.org/10.5281/zenodo.14995911.